entropy

MDPI

Article

Crossovers Between Time-Bin and Energy-Time Entanglement in Homodyned Resonance Fluorescence

Ziqi Zeng [1,2,3,*], Jian Wang [1], Bang Wu [1] and Zhiliang Yuan [1]

[1] Beijing Academy of Quantum Information Sciences, Beijing 100193, China; wangjian@baqis.ac.cn (J.W.); wubang@baqis.ac.cn (B.W.); yuanzl@baqis.ac.cn (Z.Y.)
[2] Beijing National Laboratory for Condensed Matter Physics, Institute of Physics, Chinese Academy of Sciences, Beijing 100190, China
[3] University of Chinese Academy of Sciences, Beijing 100049, China
* Correspondence: zengzq@baqis.ac.cn

Abstract

We theoretically investigate photonic entanglement generated by homodyning resonance fluorescence from a two-level emitter with a phase-locked laser field. Under weak excitation, increasing the relative laser-field amplitude produces crossovers from time-bin to energy–time and back to time-bin entanglement. The intermediate energy–time regime occurs near amplitude matching, where destructive interference suppresses the single-photon component, allowing the two-photon contributions to dominate the coincidence signal. We evaluate the resulting photon statistics and first-order coherence and characterize the entanglement through violations of the CHSH Bell inequality in a Franson interferometer. This scheme provides a route to controlling photonic entanglement through linear optics and coherent interference.

Keywords: quantum entanglement; resonance fluorescence; Franson interference

1. Introduction

Quantum entanglement is a fundamental resource in quantum information science [1,2], underpinning applications in quantum communication [3–5], quantum computation [6–8], and quantum metrology [9]. Photonic entanglement is conventionally generated through spontaneous parametric down-conversion (SPDC) and other nonlinear optical processes [10–12], which have provided a highly successful platform for quantum optics and photonic quantum information processing [13–16].

A conceptually different route is offered by resonance fluorescence (RF) from a coherently driven two-level emitter. RF-based entanglement has been explored through several approaches, including single-photon path entanglement [17], spectral filtering [18,19], and interferometric schemes [20]. In the weak-excitation (Heitler) regime, RF exhibits strong photon antibunching on the timescale of the radiative lifetime while retaining phase coherence with the driving laser and inheriting its narrow linewidth [21–26]. In the description adopted here, this coexistence of single-photon character and optical phase coherence provides a natural basis for engineering quantum states through interference.

Recently, self-homodyne interference of RF in an asymmetric Mach–Zehnder interferometer (AMZI) has been demonstrated as an all-linear-optical route to entanglement synthesis [20]. Destructive interference suppresses the single-photon component, allowing the surviving two-photon components to exhibit high-visibility Franson interference [27] and violate the Clauser–Horne–Shimony–Holt (CHSH) Bell inequality [28]. Interference of

Check for updates

Academic Editor: Alberto Porzio

Received: 30 September 2026
Revised: 16 November 2026
Accepted: 22 November 2026
Published: 24 November 2026

Copyright: © 2026 by the authors. Licensee MDPI, Basel, Switzerland. This article is an open access article distributed under the terms and conditions of the Creative Commons Attribution (CC BY) license.

RF with a coherent laser field was originally proposed as a means of tailoring its photon-number statistics [24], and has since been used to manipulate photon correlations [29–31]. In this respect, RF–laser interference offers a complementary route to photonic-state engineering: the photon-number composition of the resulting field can be controlled by a phase-locked coherent field through linear-optical interference, rather than by nonlinear pair generation as in SPDC. Whether such tunability of RF–laser interference can also be used to generate and continuously transform photonic entanglement remains less well explored.

In this work, we theoretically investigate the entanglement generated by homodyning RF with a phase-locked coherent field and analyzing the resulting field with a Franson interferometer. We derive the coincidence correlations and the corresponding CHSH Bell parameter S. As the coherent-field amplitude is varied relative to the RF field, the system undergoes a continuous crossover from time-bin entanglement to energy–time entanglement and back to time-bin entanglement, before approaching classical coherent-field interference at high coherent-field strength. The crossover arises from photon-number-selective destructive interference, whereby different Fock-state components are suppressed at different amplitude ratios. These results establish homodyne RF as a tunable route to entanglement synthesis and suggest a pathway toward controlling higher-order multiphoton states through the same interference mechanism.

2. Theoretical Framework

2.1. Pure-State Description of Resonance Fluorescence

For a coherently driven two-level emitter under steady-state conditions, in the absence of pure dephasing and at exact resonance, the joint emitter–field state at a given time can be written as [25]

$$|\psi\rangle_{ap} = \sqrt{p_0}|0\rangle|g\rangle + \sqrt{p_1}e^{-i\omega_L t}\frac{|0\rangle|e\rangle + |1\rangle|g\rangle}{\sqrt{2}}. \tag{1}$$

Here, the subscripts a and p refer to the emitter and photonic-field subsystems, respectively. The states $|g\rangle$ and $|e\rangle$ denote the ground and excited states of the emitter, while $|0\rangle$ and $|1\rangle$ denote the vacuum and single-photon states of the fluorescence field. ω_L is the laser angular frequency. The probabilities p_0 and p_1 are given by

$$p_0 = \frac{1}{1+2\Omega^2 T_1^2}, \qquad p_1 = \frac{2\Omega^2 T_1^2}{1+2\Omega^2 T_1^2}, \tag{2}$$

with $p_0 + p_1 = 1$, where Ω is the Rabi frequency and T_1 is the radiative lifetime. The dimensionless excitation strength $\Omega^2 T_1^2$ is related to the incident laser power through $\eta_{\mathrm{ab}}\bar{n} = \Omega^2 T_1^2$, where $\bar{n}$ is the mean number of incident photons within one radiative lifetime T_1, and η_{ab} denotes the emitter absorption efficiency in the weak-drive limit. Consequently, the parameter p_1 increases with excitation power, from $p_1 \to 0$ in the Heitler regime to $p_1 \to 1$ in the strong-driving limit.

The joint state provides an intuitive picture of how RF exhibits both antibunching and first-order coherence. Its photonic subsystem is restricted to the vacuum and single-photon Fock states, ensuring perfect antibunching, $g^{(2)}(0) = 0$. Coherence between $|0\rangle|g\rangle$ and $(|0\rangle|e\rangle + |1\rangle|g\rangle)/\sqrt{2}$ establishes the phase coherence of the fluorescence field, with

$$|g^{(1)}(\tau)| = p_0 \tag{3}$$

for delays much longer than T_1 but within the coherence time of the driving laser. Thus, in the Heitler regime ($p_0 \to 1$), the long-delay first-order coherence approaches unity,

corresponding to a laser-like linewidth. As the excitation power increases, p_0 decreases and the long-delay coherence gradually diminishes.

Tracing over the emitter from the joint state yields a mixed reduced state of the fluorescence field $\rho_p = \frac{2p_0+p_1}{2}|0\rangle\langle 0| + \frac{p_1}{2}|1\rangle\langle 1| + \sqrt{\frac{p_0 p_1}{2}}(|0\rangle\langle 1| + |1\rangle\langle 0|)$. This state is exactly reproduced by passing the pure state

$$|\varphi\rangle = \sqrt{p_0}|0\rangle + \sqrt{p_1}e^{-i\omega_L t}|1\rangle \tag{4}$$

through a 3 dB loss channel and tracing over the loss mode [25]. Since normalized correlation functions are invariant under linear loss, Equation (4) can be used to represent the RF field in the linear optical and correlation analysis. For RF–laser interference, the coherent reference is treated with the same attenuation, resulting in a common factor of (1/4) in the two-photon coincidence rates, which cancels in the normalized correlations. Thus, the effective-state description correctly reproduces the normalized correlations and CHSH parameter considered here. This approach has also been successfully used to account for tunable high-order coherence in RF–laser interference [31] and Bell-inequality violations in two distinct RF schemes [17,20].

2.2. Interferometric Routes to Entanglement

Figure 1 illustrates two interferometric schemes for generating entangled states. Scheme A [Figure 1a], studied in Ref. [20], relies on self-homodyne interference of the RF field in an AMZI, where the two paths acquire a relative delay τ that is much longer than the emitter lifetime ($\tau \gg T_1$) and phase θ before recombination. Scheme B [Figure 1b], considered in the present work, instead interferes the RF field with a coherent laser state $|\mu\rangle$ at a beam splitter, with their relative phase θ and the laser amplitude providing independent control of the output state [24,31].

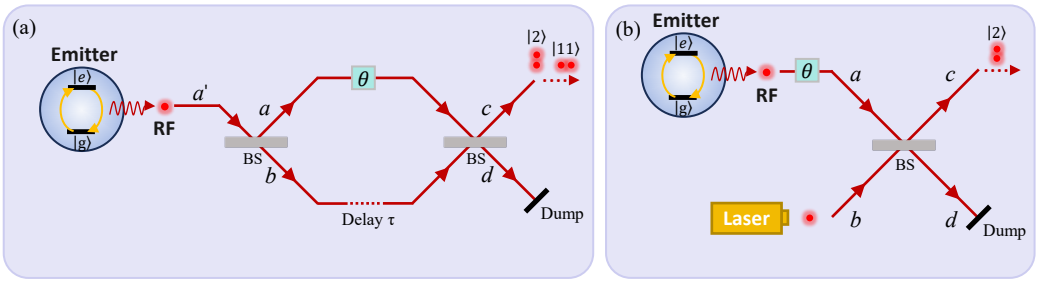


Figure 1. Two interference schemes for synthesizing entangled states from RF. (**a**) Scheme A: self-interference of RF from a coherently driven two-level emitter in an AMZI. The input at port a' is split into a short arm a with phase θ and a long arm b with delay τ, then recombined at the second BS, with output ports c and d and output state $|\varphi\rangle_{cd}$. The delay τ is chosen to be much longer than the emitter relaxation time, so that the two temporal modes can each be described by the steady-state emitter–field state of Equation (1). (**b**) Scheme B: interference of RF with a coherent laser field $|\mu\rangle$ at a BS. The coherent amplitude and the relative phase θ allow continuous control over the output state $|\Psi\rangle_{cd}$. Dashed arrows indicate subsequent routing to, e.g., a Franson interferometer for entanglement characterization.

We first consider Scheme A. As derived in Ref. [20] using the computationally effective RF state given by Equation (4), the output state at ports c and d of the AMZI is

$$
\begin{aligned}
|\varphi\rangle_{cd} = {} & p_0^{3/2}|00\rangle \\
& + \frac{e^{-i\theta}p_0\sqrt{p_1}}{\sqrt{2}}\left[(1+e^{i\theta})|01_c\rangle + (-1+e^{i\theta})|01_d\rangle + (1+e^{i\theta})|1_c0\rangle + (1-e^{i\theta})|1_d0\rangle\right] \\
& + \frac{e^{-i\theta}\sqrt{p_0}p_1}{\sqrt{2}}\left(|02_c\rangle - |02_d\rangle + |2_c0\rangle - |2_d0\rangle\right) \\
& + \frac{e^{-2i\theta}\sqrt{p_0}p_1}{2}\left[(1+e^{i\theta}+e^{2i\theta})|1_c1_c\rangle + (1-e^{i\theta}+e^{2i\theta})|1_d1_d\rangle\right. \\
& \left. + (-1-e^{i\theta}+e^{2i\theta})|1_c1_d\rangle + (-1+e^{i\theta}+e^{2i\theta})|1_d1_c\rangle\right] \\
& + \frac{e^{-i\theta}p_1^{3/2}}{2}\left(|1_c2_c\rangle - |1_c2_d\rangle + |1_d2_c\rangle - |1_d2_d\rangle\right) \\
& + \frac{e^{-2i\theta}p_1^{3/2}}{2}\left(-|2_c1_d\rangle + |2_c1_c\rangle + |2_d1_d\rangle - |2_d1_c\rangle\right),
\end{aligned}
\tag{5}
$$

where $|n_\alpha m_\beta\rangle$ denotes n photons in the early temporal mode at port α and m photons in the late temporal mode at port β, with $\alpha, \beta \in \{c, d\}$. This time-bin distinction is necessary because the AMZI introduces a relative delay τ between the long and short arms. For brevity, the common phase factor $e^{-i\omega_L t}$ has been omitted in the derivation. We write the vacuum as 0 when the corresponding mode is empty. For example, $|2_c0\rangle$ means two photons in the early mode at port c and vacuum in the late mode, while $|02_c\rangle$ means vacuum in the early mode and two photons in the late mode at port c.

With this notation, Equation (5) shows that at $\theta = \pi$ the single-photon terms $|01_c\rangle$ and $|1_c0\rangle$ vanish at port c, since their amplitudes contain the factor $1 + e^{i\theta}$. The two-photon contributions then dominate, comprising both the simultaneous pairs $|2_c0\rangle$ and $|0_c2_c\rangle$ and the time-separated pair $|1_c1_c\rangle$. The entanglement in Scheme A is accessible through temporal post-selection, since the simultaneous $|2\rangle$ and time-separated $|11\rangle$ sectors coexist and are distinguished only by their coincidence-time difference [20]. A cleaner source would retain the simultaneous two-photon component while eliminating the $|11\rangle$ sector, thereby producing entanglement from a single $|2\rangle$ sector. As shown below, this can be achieved by interfering RF with a coherent laser field.

2.3. Interference Between Resonance Fluorescence and a Coherent Field

In Scheme B, the RF state of Equation (4) is homodyned with a coherent laser state $|\mu\rangle$ at a 50/50 beam splitter: the two fields share the same central frequency and are phase-locked with relative phase θ. We define the relative field amplitude $F = \sqrt{\mu p_0 / p_1}$ and, for compactness, $\lambda = F\sqrt{p_1/(2p_0)}$. Using the general expression derived in Ref. [31], the output state at ports c and d becomes

$$
\begin{aligned}
|\Psi\rangle_{cd} = {} & e^{-\frac{F^2 p_1}{2p_0}}\sqrt{p_0}\,|0\rangle \\
& + e^{-\frac{F^2 p_1}{2p_0}}\sqrt{\frac{p_1}{2}}\sum_{k=0}^{\infty}\frac{\lambda^k}{\sqrt{(k+1)!}}\left[\left(F + e^{i\theta}(k+1)\right)|k+1\rangle_c|0\rangle_d + \left(F - e^{i\theta}(k+1)\right)|0\rangle_c|k+1\rangle_d\right] \\
& + e^{-\frac{F^2 p_1}{2p_0}}\sqrt{\frac{p_1}{2}}\sum_{k=1}^{\infty}\sum_{s=0}^{k-1}\frac{\lambda^k}{\sqrt{(s+1)!(k-s)!}}\left[F + e^{i\theta}(2s+1-k)\right]|s+1\rangle_c|k-s\rangle_d,
\end{aligned}
\tag{6}
$$

where $|s+1\rangle_c|k-s\rangle_d$ denotes a total of $n = k+1$ photons in the same temporal mode, with $s+1$ photons at port c and $k-s$ photons at port d. The first summation describes all photons exiting through a single output port, while the second describes photons distributed between both ports, with at least one photon in each.

To expose the interference structure embedded in Equation (6), we first consider the terms $|n\rangle_c|0\rangle_d$, in which all photons exit through port c. Their probability amplitudes are

proportional to $A_n = F + ne^{i\theta}$, with $n \geq 1$. At $\theta = \pi$, this reduces to $A_n = F - n$, giving a photon-number-selective cancellation condition at $F = n$. At $F = 1$, the coherent-field contribution to A_1 cancels that from the RF field, suppressing the single-photon component at port c. This is analogous to the first-order interference of fluorescence photons in Scheme A: both schemes retain a two-photon contribution in the same temporal mode at a single output port. As F increases from 1 toward 2, the single-photon amplitude regains strength. At $F = 2$, its coefficient is $A_1 = 2 - 1 = 1$, while the coherent-field and mixed RF–laser contributions to A_2 cancel, eliminating the $|2\rangle_c|0\rangle_d$ term. The resulting output can become strongly antibunched, with its nonvacuum population dominated by the single-photon component.

The cancellation conditions $A_n = 0$ derived above are exact for the selected terms $|n\rangle_c|0\rangle_d$; the full photon-number distribution at port c also receives contributions from the second summation, in which both output ports are populated. Nevertheless, these additional terms are negligible in the weak-drive limit ($p_0 \to 1$), so the above discussion captures the leading behavior.

2.4. Continuous Control of Photon-Number Statistics

To examine how interference between the RF and coherent fields affects the photon statistics, we now evaluate the zero-delay second-order correlation function $g^{(2)}(0)$ of the output field. As illustrated in Figure 2a, the RF and the coherent laser are mixed at a BS, and the output channel c is sent into a Hanbury Brown–Twiss (HBT) setup. The measurement records the single-count rate C_1 and the zero-delay coincidence rate C_2, from which $g^{(2)}(0) = C_2/C_1^2$ is obtained, where C_1^2 is the baseline count rate for independent photon arrivals. To calculate $g^{(2)}(0)$ theoretically, we write the joint quantum state of the laser and RF fields at the input ports

$$|\Psi\rangle_{in} = |\varphi_a\rangle \otimes |\varphi_b\rangle = \left(\sqrt{p_0}|0\rangle_a + \sqrt{p_1}e^{i\theta}|1\rangle_a\right) \otimes |\mu\rangle_b, \tag{7}$$

where $\sqrt{p_0}$ and $\sqrt{p_1}$ represent the magnitudes of the quantum probability amplitudes ($p_0 + p_1 = 1$), $|\mu\rangle = e^{-\mu/2}\sum_{n=0}^{\infty}(\sqrt{\mu})^n/\sqrt{n!}\,|n\rangle$ represents the coherent state with mean photon number μ, and θ is the relative phase between the two input fields.

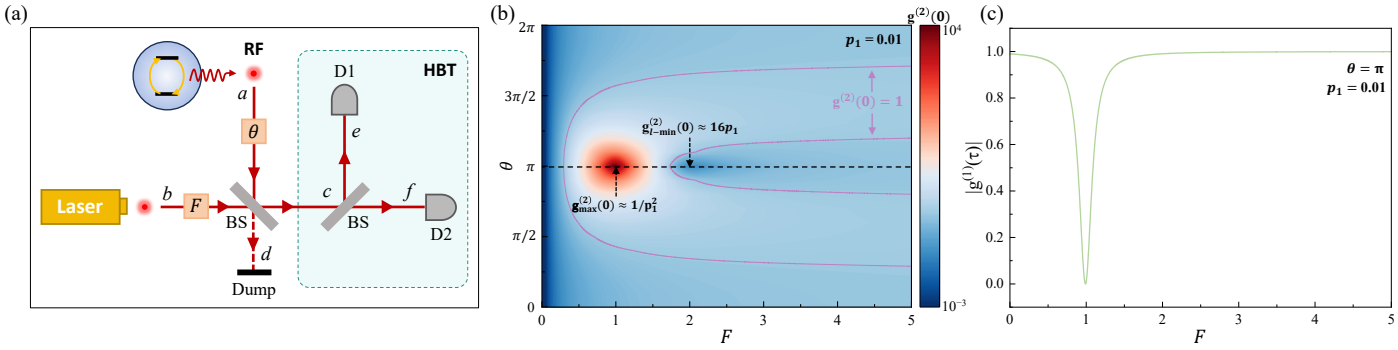


Figure 2. Photon-number correlations and first-order coherence in RF–laser interference. (**a**) Schematic of the second-order correlation measurement. The RF and coherent laser fields interfere at the first BS with relative phase θ and amplitude F. The interference output is directed to an HBT setup to measure $g^{(2)}(0)$. (**b**) Color map of the zero-delay second-order correlation function $g^{(2)}(0)$ as a function of F and θ for $p_1 = 0.01$. The color scale is logarithmic. The purple curves mark the contour $g^{(2)}(0) = 1$, separating bunched and antibunched regions. The black dashed line indicates the $\theta = \pi$ cross section, where the homodyne interference is strongest. Along this line, $g^{(2)}(0)$ reaches a superbunching maximum near $(F, \theta) = (1, \pi)$, with $g^{(2)}_{\max}(0) \approx 1/p_1^2$, and a local antibunching minimum near $(F, \theta) = (2, \pi)$, with $g^{(2)}_{l\text{-min}}(0) \approx 16p_1$. (**c**) First-order coherence $|g^{(1)}(\tau)|$ as a function of F for $\theta = \pi$ and $p_1 = 0.01$.

Firstly, we calculate the single-count rate C_1 and the zero-delay coincidence rate C_2 from the input states above (the detailed derivation is given in the Appendix A)

$$C_1 = \frac{p_1}{4} + \frac{\mu}{4} + \frac{\sqrt{p_0 p_1 \mu}}{2} \cos\theta, \tag{8}$$

$$C_2 = \frac{\mu^2}{16} + \frac{p_1 \mu}{4} + \frac{\mu^{3/2}\sqrt{p_0 p_1}}{4} \cos\theta. \tag{9}$$

Substituting Equations (8) and (9) into $g^{(2)}(0) = C_2/C_1^2$ and using $F = \sqrt{\mu p_0 / p_1}$, we obtain

$$g^{(2)}(0) = \frac{F^4 + 4F^2 p_0 + 4F^3 p_0 \cos\theta}{\left(p_0 + F^2 + 2F p_0 \cos\theta\right)^2}. \tag{10}$$

Equation (10) shows that the phase dependence of $g^{(2)}(0)$ arises entirely from terms containing p_0. Since p_0 also gives the long-delay first-order coherence of the RF field [Equation (3)], this phase sensitivity weakens as the driving power increases and p_0 decreases. In the strong-drive limit ($p_0 \to 0$), the effective RF state approaches a pure single-photon state and the phase dependence vanishes. This directly links the phase-dependent control of photon statistics to the first-order coherence of RF.

With Equation (10), we analyze $g^{(2)}(0)$ as a function of the amplitude F and phase θ under weak excitation of $p_1 = 0.01$. This choice retains a high degree of first-order coherence, $|g^{(1)}| = 0.99$, which is essential for effective homodyne interference, while maintaining a practically useful photon flux. For example, for an emitter with $T_1 = 56$ ps [32], $p_1 = 0.01$ corresponds to an emitted RF photon flux of approximately 9×10^7 s^{-1}, or a collected flux of about 9×10^6 s^{-1} for a modest collection efficiency of 10%.

Figure 2b presents $g^{(2)}(0)$ as a two-dimensional color map over the relative field amplitude F and relative phase θ for $p_1 = 0.01$. The map is symmetric about $\theta = \pi$, where destructive homodyne interference is strongest. The purple contours mark $g^{(2)}(0) = 1$, separating regions with bunched statistics, $g^{(2)}(0) > 1$, from those with antibunched statistics, $g^{(2)}(0) < 1$. At $F = 0$, corresponding to pure RF input, $g^{(2)}(0) = 0$ for all θ, reflecting the antibunched character of RF. As F increases from zero, the coherent-field contribution becomes more significant and the statistics generally evolve toward the Poissonian limit, $g^{(2)}(0) = 1$.

The most pronounced features occur along the $\theta = \pi$ cross section, indicated by the black dashed line. Near $F = 1$, the coherent-field amplitude is matched to that of the RF field, so that the single-photon contributions cancel. This leaves the two-photon component relatively enhanced and produces a superbunching maximum, with $g^{(2)}_{\max}(0) \approx 1/p_1^2$. Near $F = 2$, the destructive-interference condition shifts to the two-photon component. Cancellation of this component produces a local antibunching minimum, with $g^{(2)}_{l\text{-min}}(0) \approx 16 p_1$. Although this antibunching resembles the pure-RF case at $F = 0$, its physical origin is different: here it results from interference-induced cancellation of the two-photon amplitude while the single-photon component remains finite.

In the weak-excitation limit $p_0 \to 1$, the nonzero stationary points along $\theta = \pi$ are exactly $F = 1$ and $F = 2$. For finite p_0, they are shifted to

$$F = \frac{3p_0 \pm \sqrt{p_0(8 - 7p_0)}}{2(2p_0 - 1)}$$

for $p_0 > 1/2$. Thus, the superbunching maximum and antibunching minimum exist as distinct extrema only when $p_0 > 1/2$; for $p_0 \leq 1/2$, the antibunching minimum disappears. The dashed $\theta = \pi$ line therefore identifies the most relevant operating condition for the following analysis.

It is useful to examine the first-order coherence, because residual phase coherence can contribute to the coincidence baseline in the subsequent Franson histogram [17]. Figure 2c shows $|g^{(1)}(\tau)|$ as a function of F under weak excitation ($p_1 = 0.01$) and $\theta = \pi$, calculated using the AMZI scheme (see Appendix B)

$$|g^{(1)}(\tau)|_{\theta=\pi} = \frac{(F-p_0)^2}{(F-p_0)^2 + p_0(1-p_0)}. \tag{11}$$

At $F = 0$, corresponding to the absence of the laser field, this expression reduces to Equation (3), with $|g^{(1)}(\tau)| = p_0$. As F increases, the coherence exhibits a pronounced dip around $F = 1$, falling to exactly zero at $F = p_0$, where the phase-coherent contributions from the RF and laser fields cancel. Beyond this point, the coherence recovers and approaches unity as the laser field increasingly dominates.

2.5. Franson Interference and Bell Nonlocality

Figure 3a shows the Franson-interferometer configuration used to probe the entanglement of the RF–laser interference field. The field is divided between two analysis AMZIs, each introducing a temporal delay $\tau \gg T_1$ and a controllable phase φ_A or φ_B, where T_1 is the radiative lifetime of the two-level emitter. The two output ports of each AMZI are monitored by single-photon detectors, allowing the four coincidence combinations required for the CHSH analysis to be recorded.

The zero-delay coincidence rate for a given pair of interferometer phases is (see Appendix C)

$$\begin{aligned}
\mathcal{C}(0)(F,\theta,\varphi_A,\varphi_B) = \frac{p_1^2}{256}\Bigg[&\Big(2+2\cos(\varphi_A-\varphi_B)\Big)\\
&+8F\cos\theta\Big(1+\cos\varphi_A+\cos\varphi_B+\cos(\varphi_A-\varphi_B)\Big)\\
&+F^2\Bigg[\left(\frac{12}{p_0}+4+4\cos 2\theta\right)+\left(\frac{8}{p_0}+8+4\cos 2\theta\right)(\cos\varphi_A+\cos\varphi_B)\\
&\qquad+\left(\frac{4}{p_0}+4+4\cos 2\theta\right)\cos(\varphi_A-\varphi_B)+8\cos(\varphi_A+\varphi_B)\Bigg]\\
&+\frac{2F^3}{p_0}\Big[8\cos\theta(1+\cos\varphi_A+\cos\varphi_B)+4\cos\theta\Big(\cos(\varphi_A-\varphi_B)+\cos(\varphi_A+\varphi_B)\Big)\Big]\\
&+\frac{4F^4}{p_0^2}(1+\cos\varphi_A)(1+\cos\varphi_B)\Bigg].
\end{aligned} \tag{12}$$

From these coincidence rates, we define the correlation function [28]

$$E(\varphi_A,\varphi_B) = \frac{\mathcal{C}(0)(\varphi_A,\varphi_B)+\mathcal{C}(0)(\varphi_A+\pi,\varphi_B+\pi)-\mathcal{C}(0)(\varphi_A+\pi,\varphi_B)-\mathcal{C}(0)(\varphi_A,\varphi_B+\pi)}{\mathcal{C}(0)(\varphi_A,\varphi_B)+\mathcal{C}(0)(\varphi_A+\pi,\varphi_B+\pi)+\mathcal{C}(0)(\varphi_A+\pi,\varphi_B)+\mathcal{C}(0)(\varphi_A,\varphi_B+\pi)}. \tag{13}$$

The CHSH Bell parameter is then

$$S = \left|E(\varphi_A,\varphi_B)-E(\varphi_A,\varphi'_B)+E(\varphi'_A,\varphi_B)+E(\varphi'_A,\varphi'_B)\right|, \tag{14}$$

where (φ_A,φ'_A) and (φ_B,φ'_B) are the two phase settings of the respective analysis interferometers (see Appendix D). The CHSH inequality imposes the classical bound $S \leq 2$. Within the assumed source and measurement model, and for the temporally post-selected coincidence events, $S > 2$ indicates that the CHSH-type parameter exceeds the classical

bound. We interpret this as evidence of nonclassical temporal correlations within the post-selected subspace, not as a loophole-free Bell-nonlocality statement.

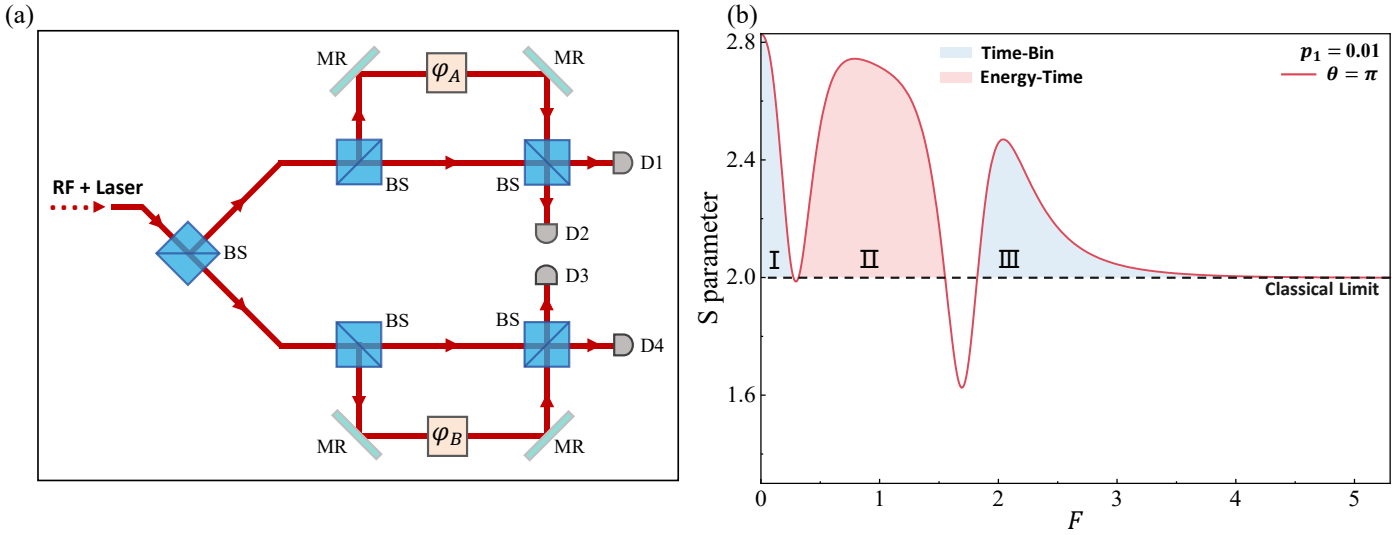


Figure 3. Analysis of the CHSH Bell parameter for RF–laser interference. (**a**) Franson-interferometer configuration. The RF–laser interference field is directed into two analysis AMZIs with relative phases φ_A and φ_B. All four output ports are monitored by single-photon detectors, allowing simultaneous measurement of the four coincidence combinations used to construct the CHSH parameter S. (**b**) S as a function of the relative field amplitude F for $\theta = \pi$ and $p_1 = 0.01$, where the black dashed line indicates the classical limit $S = 2$. The shaded regions I and III correspond to time-bin entanglement, while region II corresponds to energy–time entanglement.

To reveal entanglement crossovers, we first examine the simplest analytical limit $p_0 \to 1$ at the maximally interfering phase $\theta = \pi$. In this limit, the absolute coincidence rate is proportional to p_1^2, but its normalized phase dependence, and hence the CHSH Bell parameter, remain finite and well defined. The essential evolution is captured by four representative values of the relative amplitude: $F = 0$, $F = 1$, $F = 2$, and $F \to \infty$.

At $F = 0$, corresponding to pure RF, Equation (12) reduces to

$$\mathcal{C}(0)(\varphi_A, \varphi_B)|_{F=0} = \frac{p_1^2}{128}[1 + \cos(\varphi_A - \varphi_B)]. \tag{15}$$

The coincidence rate depends on the phase difference $\varphi_A - \varphi_B$, arising from interference between the indistinguishable long–short and short–long paths. In the ideal postselected two-photon sector, this phase-difference dependence corresponds to the time-bin state $((|E\rangle_A|L\rangle_B + |L\rangle_A|E\rangle_B)/\sqrt{2})$, where A and B label the two receiving channels, and E and L denote early and late temporal modes separated by the analyzer delay. This corresponds to time-bin entanglement and yields the maximal Bell violation $S = 2\sqrt{2}$.

At $F = 1$, destructive interference cancels the single-photon component and the simultaneous two-photon component becomes dominant. The coincidence rate becomes

$$\mathcal{C}(0)(\varphi_A, \varphi_B)|_{F=1} = \frac{p_1^2}{128}[1 + \cos(\varphi_A + \varphi_B)]. \tag{16}$$

The dependence now changes from the phase difference to the phase sum $\varphi_A + \varphi_B$, corresponding to energy–time entanglement generated by interference between the short–short and long–long two-photon paths. This phase-sum dependence corresponds to the energy–time coherence represented by $((|E\rangle_A|E\rangle_B + |L\rangle_A|L\rangle_B)/\sqrt{2})$, with the two terms

denoting coherent pair alternatives selected by the analyzer delay. The Bell parameter again reaches $S = 2\sqrt{2}$.

At $F = 2$, the simultaneous two-photon component is canceled and the field becomes strongly antibunched. The coincidence rate returns to

$$\mathcal{C}(0)(\varphi_A, \varphi_B)|_{F=2} = \frac{p_1^2}{128}[1 + \cos(\varphi_A - \varphi_B)], \tag{17}$$

recovering the same phase-difference dependence as for pure RF. The system therefore returns to time-bin entanglement, with $S = 2\sqrt{2}$.

Finally, in the limit $F \to \infty$, the coherent field dominates and the coincidence rate factorizes as

$$\mathcal{C}(0)(\varphi_A, \varphi_B)|_{F\to\infty} \propto (1 + \cos\varphi_A)(1 + \cos\varphi_B). \tag{18}$$

The responses of the two analysis interferometers are then independent, corresponding to classical coherent-state interference, and the Bell parameter approaches $S = 2$.

Together, these four limits reveal the sequence of regimes controlled by the relative coherent-field amplitude F: time-bin entanglement at $F = 0$, energy–time entanglement at $F = 1$, recovered time-bin entanglement at $F = 2$, and finally classical coherent-field interference in the limit $F \to \infty$. The first three regimes correspond to entangled two-photon correlations, while the last represents the loss of nonlocal correlations as the coherent field dominates.

Having established the limiting behavior, we now evaluate the full CHSH parameter for a practical weak excitation, $p_1 = 0.01$ ($p_0 = 0.99$). Figure 3b shows that the same sequence of regimes remains visible in the finite-excitation calculation, although the extrema of S are reduced relative to the ideal $p_0 \to 1$ case, except at $F = 0$. Region I corresponds to the RF-dominated time-bin regime. Starting from $S = 2\sqrt{2}$ at $F = 0$, the Bell parameter decreases rapidly and reaches a first valley near $F \simeq 0.30$, where it falls slightly below the classical bound $S = 2$. Region II corresponds to the energy–time-dominated regime. In this region, S rises again and reaches a broad maximum of $S \simeq 2.74$ at $F \simeq 0.79$, close to the single-photon cancellation condition near $F = 1$. As F is increased further, S decreases to a second valley near $F \simeq 1.69$. Region III corresponds to the recovered time-bin regime. Here, S increases again and reaches a smaller maximum of $S \simeq 2.47$ around $F \simeq 2.04$, close to the two-photon cancellation condition near $F = 2$. For still larger F, the coherent field dominates and S gradually approaches the classical bound $S = 2$.

The displacement of the local maxima from exactly $F = 1$ and $F = 2$ does not change the underlying interference mechanism. These two values still identify the cancellation of the selected single- and two-photon amplitudes, respectively. At finite p_1, however, the full Franson coincidence signal also contains additional Fock-state contributions from the laser input, which modify the optimized Bell parameter and shift the maxima of S. Thus, Figure 3b should be viewed as a finite-excitation realization of the ideal crossover sequence discussed above, rather than as a different mechanism. A reference simulation in the ideal weak-excitation limit, $p_1 = 10^{-6}$, which more clearly reveals the crossover sequence and the corresponding Franson coincidence histograms, is provided in Appendix E (Figure A1).

The recovery of time-bin entanglement in Region III is not unconditional. It relies on the antibunching associated with two-photon cancellation near $F = 2$. As discussed in Figure 2, this antibunching minimum exists only for $p_0 > 1/2$. For $p_0 < 1/2$, the antibunching minimum disappears, and the recovered time-bin-entangled regime is correspondingly lost.

3. Conclusions

In this work, we have revealed that the destructive interference between RF and a coherent laser field provides a viable mechanism for generating and continuously tuning entanglement. By adjusting the coherent amplitude F, the system can be navigated across distinct entanglement regimes: from time-bin entanglement at $F = 0$, through energy-time entanglement around $F = 1$, back to time-bin entanglement around $F = 2$, and eventually to classical coherence as $F \to \infty$. This crossover demonstrates that a single experimental configuration, based solely on passive linear optics and coherent field mixing, can realize qualitatively different classes of two-photon correlations through a single external parameter. The selective suppression of photon-number components via destructive interference is the underlying mechanism that enables this tunability. Our results establish homodyned RF as a versatile platform for controlled quantum state engineering, with potential implications for integrated photonic quantum information processing. Furthermore, the photon-number-selective interference mechanism may also motivate future studies of higher-order correlations and the conditions under which they can give rise to multiphoton entanglement. A detailed investigation of these extensions is beyond the scope of the present work and will be addressed in future studies.

Author Contributions: Conceptualization, Z.Z. and Z.Y.; resources, B.W. and Z.Y.; writing—original draft preparation, Z.Z.; writing—review and editing, J.W., B.W. and Z.Z.; supervision, Z.Y. All authors have read and agreed to the published version of the manuscript.

Funding: This research was funded by the Quantum Science and Technology-National Science and Technology Major Project (No. 2024ZD0302500), the National Natural Science Foundation of China under grants (12494604 and 12504410), and Beijing Academy of Quantum Information Sciences (Grant No. Y26NG262802).

Data Availability Statement: The data presented in this paper are available after contacting the corresponding author.

Conflicts of Interest: The authors declare no conflicts of interest.

Appendix A. Derivation of the Second-Order Correlation Function $g^{(2)}(0)$

As the setup shown in Figure 2a, the input state at time t is the product of two independent modes,

$$|\Psi\rangle = |\varphi_a\rangle \otimes |\varphi_b\rangle\,, \tag{A1}$$

$$|\varphi_a\rangle = \sqrt{p_0}\,|0\rangle_a + \sqrt{p_1}\,e^{i\theta}\,|1\rangle_a\,, \qquad p_0 + p_1 = 1, \tag{A2}$$

$$|\varphi_b\rangle = e^{-\mu/2}\sum_{n=0}^{\infty}\frac{(\sqrt{\mu})^n}{\sqrt{n!}}\,|n\rangle_b\,, \tag{A3}$$

where $|\varphi_b\rangle$ is a coherent state of real amplitude $\sqrt{\mu}$ (mean photon number $\mu = (p_1/p_0)\,F^2$, where the dimensionless parameter F controls the relative amplitude of the coherent field). In the experiment, one output of a first 50:50 beam splitter is directed to a Hanbury Brown–Twiss (HBT) interferometer. The field operator of that port is $c = (a + b)/\sqrt{2}$, and we use the shorthand $a \equiv a_t$, $b \equiv b_t$. Inside the HBT setup, mode c is further split by a second 50:50 beam splitter and the two outputs are monitored by single-photon detectors D_1 and D_2. For ideal detectors, the single-count rate of one detector is proportional to $\langle c^\dagger c\rangle/2$,

while the coincidence rate between the two detectors is proportional to $\langle c^{\dagger 2} c^2 \rangle / 4$. It is therefore convenient to introduce the scaled operators

$$\hat{O}_1 \equiv \frac{c}{\sqrt{2}} = \frac{a+b}{2}, \qquad \hat{O}_2 \equiv \frac{c^2}{2} = \frac{a^2 + 2ab + b^2}{4}, \tag{A4}$$

whose expectation values directly yield

$$C_1 = \langle \Psi | \hat{O}_1^\dagger \hat{O}_1 | \Psi \rangle = \frac{1}{2} \langle c^\dagger c \rangle, \qquad C_2 = \langle \Psi | \hat{O}_2^\dagger \hat{O}_2 | \Psi \rangle = \frac{1}{4} \langle c^{\dagger 2} c^2 \rangle. \tag{A5}$$

The normalized second-order correlation function at zero delay then takes the compact form

$$g^{(2)}(0) = \frac{C_2}{C_1^2}. \tag{A6}$$

We first evaluate C_1. For the single-photon operator $\hat{O}_1 = (a+b)/2$, using $a\,|\varphi_a\rangle = \sqrt{p_1} e^{i\theta}\,|0\rangle_a$ and the coherent-state property $b\,|\varphi_b\rangle = \sqrt{\mu}\,|\varphi_b\rangle$, we obtain

$$\hat{O}_1\,|\Psi\rangle = \frac{1}{2}\Big[\sqrt{p_1} e^{i\theta}\,|0\rangle_a\,|\varphi_b\rangle + \sqrt{\mu}\,|\varphi_a\rangle\,|\varphi_b\rangle\Big]. \tag{A7}$$

Defining the normalized states $|X\rangle = |0\rangle_a\,|\varphi_b\rangle$ and $|Y\rangle = |\varphi_a\rangle\,|\varphi_b\rangle$, with $\langle X|Y\rangle = \sqrt{p_0}$, we have

$$\hat{O}_1\,|\Psi\rangle = \frac{\sqrt{p_1}}{2} e^{i\theta}\,|X\rangle + \frac{\sqrt{\mu}}{2}\,|Y\rangle\,. \tag{A8}$$

The single-count rate $C_1 = |\hat{O}_1\,|\Psi\rangle\,|^2$ then becomes

$$C_1 = \frac{p_1}{4}\langle X|X\rangle + \frac{\mu}{4}\langle Y|Y\rangle + 2\,\mathrm{Re}\Big[\frac{\sqrt{p_1}}{2} e^{i\theta} \frac{\sqrt{\mu}}{2} \langle X|Y\rangle\Big] \tag{A9}$$

$$= \frac{p_1}{4} + \frac{\mu}{4} + \frac{\sqrt{p_0 p_1 \mu}}{2}\cos\theta. \tag{A10}$$

We now turn to C_2. For the two-photon operator $\hat{O}_2 = (a^2 + 2ab + b^2)/4$, since $|\varphi_a\rangle$ contains at most one photon, $a^2\,|\varphi_a\rangle = 0$, so $a^2\,|\Psi\rangle = 0$. The cross terms give

$$ab\,|\Psi\rangle = ba\,|\Psi\rangle = \sqrt{p_1 \mu}\, e^{i\theta}\;|0\rangle_a\,|\varphi_b\rangle = \sqrt{p_1\mu}\, e^{i\theta}\,|X\rangle\,, \tag{A11}$$

and the b^2 term yields

$$b^2\,|\Psi\rangle = \mu\;|\varphi_a\rangle\,|\varphi_b\rangle = \mu\,|Y\rangle\,. \tag{A12}$$

Assembling these results,

$$\hat{O}_2\,|\Psi\rangle = \frac{\sqrt{p_1\mu}}{2} e^{i\theta}\,|X\rangle + \frac{\mu}{4}\,|Y\rangle\,. \tag{A13}$$

The coincidence rate $C_2 = |\hat{O}_2\,|\Psi\rangle\,|^2$ then becomes

$$C_2 = \frac{p_1\mu}{4}\langle X|X\rangle + \frac{\mu^2}{16}\langle Y|Y\rangle + 2\,\mathrm{Re}\Big[\frac{\sqrt{p_1\mu}}{2} e^{i\theta} \frac{\mu}{4} \langle X|Y\rangle\Big] \tag{A14}$$

$$= \frac{p_1\mu}{4} + \frac{\mu^2}{16} + \frac{\mu^{3/2}\sqrt{p_0 p_1}}{4}\cos\theta. \tag{A15}$$

Substituting C_1 and C_2 into $g^{(2)}(0) = C_2/C_1^2$ yields

$$g^{(2)}(0) = \frac{\frac{\mu^2}{16} + \frac{p_1\mu}{4} + \frac{\mu^{3/2}\sqrt{p_0 p_1}}{4}\cos\theta}{\left(\frac{p_1}{4} + \frac{\mu}{4} + \frac{\sqrt{p_0 p_1 \mu}}{2}\cos\theta\right)^2}. \tag{A16}$$

The interference terms in C_1 and C_2 scale as $\sqrt{p_0 p_1 \mu}$ and $\mu^{3/2}\sqrt{p_0 p_1}$, respectively. In both cases, the presence of $\cos\theta$ shows that the phase of the single-photon component in mode a can interfere with the coherent amplitude of mode b, provided a vacuum component exists ($p_0 p_1 > 0$). When mode a is a pure single-photon state ($p_0 = 0$), the interference vanishes and only the incoherent background remains. This behavior highlights the role of the vacuum amplitude in sustaining phase coherence in such hybrid quantum–classical states.

Substituting $\mu = F^2 p_1/p_0$ into the above expression and multiplying both numerator and denominator by $16p_0^2/p_1^2$, we obtain the simplified form

$$g^{(2)}(0) = \frac{F^4 + 4F^2 p_0 + 4F^3 p_0 \cos\theta}{(p_0 + F^2 + 2F p_0 \cos\theta)^2}, \tag{A17}$$

which is exactly Equation (10) in the main text. For $\theta = \pi$, the above equation reduces to

$$g^{(2)}(0) = \frac{F^4 - 4p_0 F^3 + 4p_0 F^2}{(F^2 - 2p_0 F + p_0)^2}. \tag{A18}$$

Differentiating with respect to F and setting the derivative to zero gives

$$4p_0 F\Big[(2p_0 - 1)F^2 - 3p_0 F + 2p_0\Big] = 0. \tag{A19}$$

Apart from the trivial stationary point $F = 0$, which corresponds to the pure RF input with $g^{(2)}(0) = 0$, the non-zero stationary points satisfy

$$(2p_0 - 1)F^2 - 3p_0 F + 2p_0 = 0. \tag{A20}$$

Its solutions are

$$F = \frac{3p_0 \pm \sqrt{p_0(8 - 7p_0)}}{2(2p_0 - 1)} \qquad (p_0 > 1/2). \tag{A21}$$

For $p_0 > 1/2$, there are two positive stationary points. The smaller F corresponds to a maximum of $g^{(2)}(0)$ (superbunching peak), while the larger F corresponds to a minimum (antibunching dip). The extremal values of $g^{(2)}(0)$ are obtained in closed form as

$$g^{(2)}_{\max}(p_0) = \frac{2\left[88p_0^3 - 163p_0^2 + 52p_0 + 24 - \left(8p_0^2 - 41p_0 + 32\right)\Delta\right]}{\left[-4p_0^2 - p_0 + 6 - (5 - 4p_0)\Delta\right]^2}, \tag{A22}$$

$$g^{(2)}_{\min}(p_0) = \frac{2\left[88p_0^3 - 163p_0^2 + 52p_0 + 24 + \left(8p_0^2 - 41p_0 + 32\right)\Delta\right]}{\left[-4p_0^2 - p_0 + 6 + (5 - 4p_0)\Delta\right]^2}, \tag{A23}$$

where

$$\Delta = \sqrt{p_0(8 - 7p_0)}. \tag{A24}$$

In the weak-excitation limit $p_0 \to 1$, writing $p_1 = 1 - p_0 \ll 1$, the stationary-point equation reduces to $F^2 - 3F + 2 = 0$, i.e., $F = 1$ and $F = 2$, corresponding to the superbunch-

ing peak and antibunching dip, respectively, in agreement with Figure 2b. Substituting these two values into the above equation, the extremal values of $g^{(2)}(0)$ simplify to

$$g^{(2)}_{\max} \approx \frac{1}{p_1^2}, \qquad g^{(2)}_{\min} \approx 16p_1. \tag{A25}$$

Appendix B. Calculation of $|g^{(1)}(\tau)|$ Versus F for $\theta = \pi$

Experimentally, first-order coherence function $|g^{(1)}(\tau)|$ can be measured through an AMZI. We consider one AMZI of the Franson interferometer shown in Figure 3a of the main text, whose two arms have a relative time delay τ; its relative phase ϕ_A is scanned, and the single counts $C(\phi_A)$ at one output port are recorded. The normalized fringe contrast gives the interference visibility $V \equiv |g^{(1)}(\tau)|$. The input state consists of the resonance-fluorescence field (mode a) and the coherent laser field (mode b), each containing early and late time bins, and is written as a direct product

$$|\Psi_{\text{in}}\rangle = |\phi_a\rangle_{t-\tau} \otimes |\phi_a\rangle_t \otimes |\phi_b\rangle_{t-\tau} \otimes |\phi_b\rangle_t, \tag{A26}$$

where

$$|\phi_a\rangle = \sqrt{p_0}|0\rangle + \sqrt{p_1}e^{i\theta}|1\rangle, \qquad p_0 + p_1 = 1, \tag{A27}$$

$$|\phi_b\rangle = e^{-\mu/2}\sum_{n=0}^{\infty}\frac{(\sqrt{\mu})^n}{\sqrt{n!}}|n\rangle_b \equiv |\sqrt{\mu}\rangle. \tag{A28}$$

Here, $|\phi_a\rangle_{t-\tau}$ and $|\phi_a\rangle_t$ denote the resonance-fluorescence field in the early and late time bins, respectively, while $|\phi_b\rangle_{t-\tau}$ and $|\phi_b\rangle_t$ denote the coherent laser field in the early and late time bins. Consider the operator

$$\hat{O} = a_{t-\tau} + b_{t-\tau} + e^{i\phi_A}a_t + e^{i\phi_A}b_t. \tag{A29}$$

The single-count rate is defined as

$$C(\phi_A) = \langle\Psi_{\text{in}}|\hat{O}^\dagger\hat{O}|\Psi_{\text{in}}\rangle = |\hat{O}|\Psi_{\text{in}}\rangle|^2. \tag{A30}$$

For a term-by-term calculation, we write

$$\hat{O} = A + B + C + D, \tag{A31}$$

where

$$A = a_{t-\tau}, \qquad B = b_{t-\tau}, \qquad C = e^{i\phi_A}a_t, \qquad D = e^{i\phi_A}b_t. \tag{A32}$$

Acting on the input state gives four terms

$$T_1 = A|\Psi_{\text{in}}\rangle = \sqrt{p_1}e^{i\theta}|0\rangle_{a,t-\tau}|\phi_a\rangle_t|\phi_b\rangle_{t-\tau}|\phi_b\rangle_t, \tag{A33}$$

$$T_2 = B|\Psi_{\text{in}}\rangle = \sqrt{\mu}|\phi_a\rangle_{t-\tau}|\phi_a\rangle_t|\phi_b\rangle_{t-\tau}|\phi_b\rangle_t, \tag{A34}$$

$$T_3 = C|\Psi_{\text{in}}\rangle = e^{i\phi_A}\sqrt{p_1}e^{i\theta}|\phi_a\rangle_{t-\tau}|0\rangle_{a,t}|\phi_b\rangle_{t-\tau}|\phi_b\rangle_t, \tag{A35}$$

$$T_4 = D|\Psi_{\text{in}}\rangle = e^{i\phi_A}\sqrt{\mu}|\phi_a\rangle_{t-\tau}|\phi_a\rangle_t|\phi_b\rangle_{t-\tau}|\phi_b\rangle_t. \tag{A36}$$

Therefore,

$$O|\Psi_{\text{in}}\rangle = T_1 + T_2 + T_3 + T_4. \tag{A37}$$

The single-count rate is

$$C(\phi_A) = \sum_{i=1}^{4}\sum_{j=1}^{4}\langle T_i|T_j\rangle. \tag{A38}$$

Evaluating the 16 inner products term by term and using

$$\langle 0|\phi_a\rangle = \sqrt{p_0}, \qquad \langle \phi_a|\phi_a\rangle = 1, \qquad \langle \phi_b|\phi_b\rangle = 1, \tag{A39}$$

we obtain

$$\begin{aligned}
&\langle T_1|T_1\rangle = p_1, && \langle T_1|T_2\rangle = \sqrt{p_0 p_1 \mu}\, e^{-i\theta},\\
&\langle T_1|T_3\rangle = p_0 p_1 e^{i\phi_A}, && \langle T_1|T_4\rangle = \sqrt{p_0 p_1 \mu}\, e^{i(\phi_A-\theta)},\\
&\langle T_2|T_1\rangle = \sqrt{p_0 p_1 \mu}\, e^{i\theta}, && \langle T_2|T_2\rangle = \mu,\\
&\langle T_2|T_3\rangle = \sqrt{p_0 p_1 \mu}\, e^{i(\phi_A+\theta)}, && \langle T_2|T_4\rangle = \mu e^{i\phi_A},\\
&\langle T_3|T_1\rangle = p_0 p_1 e^{-i\phi_A}, && \langle T_3|T_2\rangle = \sqrt{p_0 p_1 \mu}\, e^{-i(\phi_A+\theta)},\\
&\langle T_3|T_3\rangle = p_1, && \langle T_3|T_4\rangle = \sqrt{p_0 p_1 \mu}\, e^{-i\theta},\\
&\langle T_4|T_1\rangle = \sqrt{p_0 p_1 \mu}\, e^{-i(\phi_A-\theta)}, && \langle T_4|T_2\rangle = \mu e^{-i\phi_A},\\
&\langle T_4|T_3\rangle = \sqrt{p_0 p_1 \mu}\, e^{i\theta}, && \langle T_4|T_4\rangle = \mu.
\end{aligned} \tag{A40}$$

Summing these 16 terms and combining the conjugate pairs, we find

$$\begin{aligned}
C(\phi_A) = {} & 2p_1 + 2\mu + 4\sqrt{p_0 p_1 \mu}\cos\theta \\
& + 2(p_0 p_1 + \mu)\cos\phi_A + 4\sqrt{p_0 p_1 \mu}\cos\phi_A \cos\theta.
\end{aligned} \tag{A41}$$

Using $F = \sqrt{\mu p_0 / p_1}$, we obtain

$$C(\phi_A) = 2p_1\left[1 + \frac{F^2}{p_0} + 2F\cos\theta + \left(p_0 + \frac{F^2}{p_0} + 2F\cos\theta\right)\cos\phi_A\right]. \tag{A42}$$

Writing

$$C(\phi_A) = A + B\cos\phi_A, \tag{A43}$$

we identify

$$A = 2(1-p_0)\left[1 + \frac{F^2}{p_0} + 2F\cos\theta\right], \tag{A44}$$

$$B = 2(1-p_0)\left[p_0 + \frac{F^2}{p_0} + 2F\cos\theta\right]. \tag{A45}$$

Since the scanned quantity is the phase ϕ_A, and the extracted visibility is

$$|g^{(1)}(\tau)| = V = \frac{C(F,0) - C(F,\pi)}{C(F,0) + C(F,\pi)} = \frac{B}{A}. \tag{A46}$$

Substituting the expressions for A and B gives

$$|g^{(1)}(\tau)| = \frac{p_0 + \dfrac{F^2}{p_0} + 2F\cos\theta}{1 + \dfrac{F^2}{p_0} + 2F\cos\theta}. \tag{A47}$$

Setting $\theta = \pi$, so that $\cos\theta = -1$, the above equation yields

$$|g^{(1)}(\tau)|_{\theta=\pi} = \frac{p_0 + \dfrac{F^2}{p_0} - 2F}{1 + \dfrac{F^2}{p_0} - 2F} = \frac{(F-p_0)^2}{(F-p_0)^2 + p_0(1-p_0)}, \tag{A48}$$

which is the general expression for $|g^{(1)}(\tau)|$ as a function of F for $\theta = \pi$. In particular, at $F = p_0$, $|g^{(1)}(\tau)|_{\theta=\pi} = 0$, indicating that the first-order coherence vanishes completely. Using the above expression, we calculate the $|g^{(1)}(\tau)|$ versus the relative field amplitude F for $p_1 = 0.01$, as shown in Figure 2c of the main text. For $F = 0$, $|g^{(1)}(\tau)|_{\theta=\pi}\big|_{F=0} = \frac{p_0^2}{p_0^2+p_0(1-p_0)} = p_0$. For $F = p_0$, $|g^{(1)}(\tau)|_{\theta=\pi}\big|_{F=p_0} = 0$.

Appendix C. Derivation of the Coincidence Rate

Considering the Franson interferometer shown in Figure 3a of the main text, the initial state consists of two spatial modes, each carrying two time bins labeled $t-\tau$ (early) and t (late), which is the same as Equation (A26). The output measurement is described by the operator

$$\hat{O} = \frac{1}{16}\left[\hat{a}_{t-\tau} + \hat{b}_{t-\tau} + e^{i\varphi_A}(\hat{a}_t + \hat{b}_t)\right]\left[\hat{a}_{t-\tau} + \hat{b}_{t-\tau} + e^{i\varphi_B}(\hat{a}_t + \hat{b}_t)\right], \tag{A49}$$

which combines the two time bins with independently tunable phases φ_A, φ_B; the prefactor $1/16$ is a convenient normalization.

The action of individual operators on the initial state follows from the simple rules

$$\hat{a}\,|\varphi_a\rangle = \sqrt{p_1}e^{i\theta}\,|0\rangle\,, \quad \hat{a}^2\,|\varphi_a\rangle = 0, \qquad \hat{b}\,|\sqrt{\mu}\rangle = \sqrt{\mu}\,|\sqrt{\mu}\rangle\,, \quad \hat{b}^2\,|\sqrt{\mu}\rangle = \mu\,|\sqrt{\mu}\rangle\,. \tag{A50}$$

Expanding $\hat{O}$ generates sixteen terms, each being a product of two annihilation operators. The result of each operator product acting on $|\Psi_{\text{in}}\rangle$ is summarized in Table A1. (For brevity, we use $u = e^{i\varphi_A}$, $v = e^{i\varphi_B}$.) We also introduce the normalized four-mode basis states to simplify the table

$$\begin{aligned}
|S_1\rangle &= |0\rangle_{t-\tau}\,|\varphi_a\rangle_t\,|\sqrt{\mu}\rangle_{t-\tau}\,|\sqrt{\mu}\rangle_t\,,\\
|S_2\rangle &= |0\rangle_{t-\tau}\,|0\rangle_t\,|\sqrt{\mu}\rangle_{t-\tau}\,|\sqrt{\mu}\rangle_t\,,\\
|S_3\rangle &= |\varphi_a\rangle_{t-\tau}\,|0\rangle_t\,|\sqrt{\mu}\rangle_{t-\tau}\,|\sqrt{\mu}\rangle_t\,,\\
|S_4\rangle &= |\varphi_a\rangle_{t-\tau}\,|\varphi_a\rangle_t\,|\sqrt{\mu}\rangle_{t-\tau}\,|\sqrt{\mu}\rangle_t\,.
\end{aligned} \tag{A51}$$

Table A1. Result of each operator product acting on $|\Psi_{\text{in}}\rangle$ (factor $1/16$ omitted).

Term	Result
1. $\hat{a}_{t-\tau}\hat{a}_{t-\tau}$	0
2. $\hat{a}_{t-\tau}\hat{b}_{t-\tau}$	$\sqrt{\mu p_1}\,e^{i\theta}\ \|S_1\rangle$
3. $\hat{a}_{t-\tau}(v\,\hat{a}_t)$	$v\,p_1 e^{i2\theta}\ \|S_2\rangle$
4. $\hat{a}_{t-\tau}(v\,\hat{b}_t)$	$\sqrt{\mu p_1}\,e^{i\theta}\,v\ \|S_1\rangle$
5. $\hat{b}_{t-\tau}\hat{a}_{t-\tau}$	$\sqrt{\mu p_1}\,e^{i\theta}\ \|S_1\rangle$
6. $\hat{b}_{t-\tau}\hat{b}_{t-\tau}$	$\mu\ \|S_4\rangle$
7. $\hat{b}_{t-\tau}(v\,\hat{a}_t)$	$\sqrt{\mu p_1}\,e^{i\theta}\,v\ \|S_3\rangle$
8. $\hat{b}_{t-\tau}(v\,\hat{b}_t)$	$\mu\,v\ \|S_4\rangle$
9. $(u\,\hat{a}_t)\hat{a}_{t-\tau}$	$u\,p_1 e^{i2\theta}\ \|S_2\rangle$
10. $(u\,\hat{a}_t)\hat{b}_{t-\tau}$	$\sqrt{\mu p_1}\,e^{i\theta}\,u\ \|S_3\rangle$
11. $(u\,\hat{a}_t)(v\,\hat{a}_t)$	0
12. $(u\,\hat{a}_t)(v\,\hat{b}_t)$	$\sqrt{\mu p_1}\,e^{i\theta}\,uv\ \|S_3\rangle$
13. $(u\,\hat{b}_t)\hat{a}_{t-\tau}$	$\sqrt{\mu p_1}\,e^{i\theta}\,u\ \|S_1\rangle$
14. $(u\,\hat{b}_t)\hat{b}_{t-\tau}$	$\mu\,u\ \|S_4\rangle$
15. $(u\,\hat{b}_t)(v\,\hat{a}_t)$	$\sqrt{\mu p_1}\,e^{i\theta}\,uv\ \|S_3\rangle$
16. $(u\,\hat{b}_t)(v\,\hat{b}_t)$	$\mu\,uv\ \|S_4\rangle$

Summing all contributions, the unnormalized output results take the compact form

$$\hat{O}\,|\Psi_{\text{in}}\rangle = \frac{1}{16}\big(C_1\,|S_1\rangle + C_2\,|S_2\rangle + C_3\,|S_3\rangle + C_4\,|S_4\rangle\big), \tag{A52}$$

with

$$\begin{aligned} C_1 &= \sqrt{\mu p_1}\, e^{i\theta}\,(2+u+v),\\ C_2 &= p_1 e^{i2\theta}\,(u+v),\\ C_3 &= \sqrt{\mu p_1}\, e^{i\theta}\,(u+v+2uv),\\ C_4 &= \mu\,(1+u)(1+v). \end{aligned} \tag{A53}$$

The experimentally measured coincidence count rate at the center zero delay is proportional to the norm squared of this unnormalized state. Denoting this rate by $\mathcal{C}(0)$, we have

$$\begin{aligned} \mathcal{C}(0) = |\hat{O}\,|\Psi_{\text{in}}\rangle\,|^2 = \frac{1}{256}\Big[\sum_{i=1}^{4}|C_i|^2 + 2\sqrt{p_0}\,\mathrm{Re}\big(C_1^*C_2 + C_1^*C_4 + C_2^*C_3 + C_3^*C_4\big)\\ + 2p_0\,\mathrm{Re}\big(C_1^*C_3 + C_2^*C_4\big)\Big]. \end{aligned} \tag{A54}$$

Here, the inner products $\langle S_i|S_j\rangle$ were evaluated using $\langle 0|\varphi_a\rangle = \sqrt{p_0}$ and $\langle\varphi_a|\varphi_a\rangle = 1$, which yields the non-trivial overlaps $\langle S_1|S_2\rangle = \langle S_1|S_4\rangle = \langle S_2|S_3\rangle = \langle S_3|S_4\rangle = \sqrt{p_0}$ and $\langle S_1|S_3\rangle = \langle S_2|S_4\rangle = p_0$.

Substituting the explicit coefficients $C_1 \ldots C_4$ and expanding yields the fully trigonometric form

$$\begin{aligned} \mathcal{C}(0)(\mu,\theta,\varphi_A,\varphi_B) = \frac{1}{256}\Big\{ & 2\mu p_1\big(6 + 4\cos\varphi_A + 4\cos\varphi_B + 2\cos(\varphi_A-\varphi_B)\big)\\ & + p_1^2\big(2 + 2\cos(\varphi_A-\varphi_B)\big)\\ & + 4\mu^2(1+\cos\varphi_A)(1+\cos\varphi_B)\\ & + 2p_0\mu p_1\big(2 + 4\cos\varphi_A + 4\cos\varphi_B + 2\cos(\varphi_A-\varphi_B) + 4\cos(\varphi_A+\varphi_B)\big)\\ & + 2\sqrt{p_0}\sqrt{\mu}\,p_1^{3/2}\Big[2\cos(\theta+\varphi_A) + 2\cos(\theta+\varphi_B) + 2\cos\theta + 2\cos\theta\cos(\varphi_A-\varphi_B)\Big]\\ & + 2\sqrt{p_0}\sqrt{\mu}\,p_1^{3/2}\Big[2(1+\cos(\varphi_A-\varphi_B))\cos\theta + 2\cos(\theta-\varphi_A) + 2\cos(\theta-\varphi_B)\Big]\\ & + 2\sqrt{p_0}\,\mu^{3/2}\sqrt{p_1}\Big[4\cos\theta + 3\cos(\theta-\varphi_A) + 3\cos(\theta-\varphi_B)\\ & \qquad + \cos(\theta+\varphi_A) + \cos(\theta+\varphi_B) + \cos(\theta-\varphi_A+\varphi_B)\\ & \qquad + \cos(\theta+\varphi_A-\varphi_B) + 2\cos(\theta-\varphi_A-\varphi_B)\Big]\\ & + 2\sqrt{p_0}\,\mu^{3/2}\sqrt{p_1}\Big[4\cos\theta + \cos(\theta-\varphi_A) + \cos(\theta-\varphi_B)\\ & \qquad + 3\cos(\theta+\varphi_A) + 3\cos(\theta+\varphi_B) + \cos(\theta-\varphi_A+\varphi_B)\\ & \qquad + \cos(\theta+\varphi_A-\varphi_B) + 2\cos(\theta+\varphi_A+\varphi_B)\Big]\\ & + 4p_0\mu p_1\big(1 + \cos\varphi_A + \cos\varphi_B + \cos(\varphi_A-\varphi_B)\big)\cos 2\theta\Big\}. \end{aligned} \tag{A55}$$

Using the definition of mean photon number $\mu = (p_1/p_0)\,F^2$, the above equation can be simplified as

$$\begin{aligned}\mathcal{C}(0)(F,\theta,\varphi_A,\varphi_B) = \frac{p_1^2}{256}\Bigg[&\Big(2+2\cos(\varphi_A-\varphi_B)\Big)\\ &+8F\cos\theta\Big(1+\cos\varphi_A+\cos\varphi_B+\cos(\varphi_A-\varphi_B)\Big)\\ &+F^2\Bigg[\left(\frac{12}{p_0}+4+4\cos 2\theta\right)+\left(\frac{8}{p_0}+8+4\cos 2\theta\right)(\cos\varphi_A+\cos\varphi_B)\\ &\qquad+\left(\frac{4}{p_0}+4+4\cos 2\theta\right)\cos(\varphi_A-\varphi_B)+8\cos(\varphi_A+\varphi_B)\Bigg]\\ &+\frac{2F^3}{p_0}\Big[8\cos\theta\big(1+\cos\varphi_A+\cos\varphi_B\big)+4\cos\theta\Big(\cos(\varphi_A-\varphi_B)+\cos(\varphi_A+\varphi_B)\Big)\Big]\\ &+\frac{4F^4}{p_0^2}(1+\cos\varphi_A)(1+\cos\varphi_B)\Bigg].\end{aligned} \tag{A56}$$

We first examine the case where the relative phase between the two input states is $\theta = \pi$. Setting $\cos\theta = -1$ and $\cos 2\theta = 1$ yields

$$\begin{aligned}\mathcal{C}(0)(F,\varphi_A,\varphi_B) = \frac{p_1^2}{256}\Bigg[&\big(2+2\cos(\varphi_A-\varphi_B)\big)\\ &-8F\big(1+\cos\varphi_A+\cos\varphi_B+\cos(\varphi_A-\varphi_B)\big)\\ &+F^2\Bigg[\left(\frac{12}{p_0}+8\right)+\left(\frac{8}{p_0}+12\right)(\cos\varphi_A+\cos\varphi_B)\\ &\qquad+\left(\frac{4}{p_0}+8\right)\cos(\varphi_A-\varphi_B)+8\cos(\varphi_A+\varphi_B)\Bigg]\\ &+\frac{2F^3}{p_0}\Big[-8\big(1+\cos\varphi_A+\cos\varphi_B\big)-4\big(\cos(\varphi_A-\varphi_B)+\cos(\varphi_A+\varphi_B)\big)\Big]\\ &+\frac{4F^4}{p_0^2}(1+\cos\varphi_A)(1+\cos\varphi_B)\Bigg].\end{aligned} \tag{A57}$$

With this phase convention fixed, we now examine the behavior of the coincidence rate as a function of the coherent amplitude F. Specifically, we consider four representative limits: $F = 0$, corresponding to pure RF; $F = 1$, for which $\mu = p_1/p_0$; $F = 2$, for which $\mu = 4p_1/p_0$; and the asymptotic limit $F \to \infty$, where the coherent field dominates. These limits reveal the distinct physical regimes of the Franson interferometer.

1. For $F = 0$, only the zeroth-order term remains; the coincidence rate reduces to

$$\mathcal{C}(0)(\varphi_A,\varphi_B) = \frac{p_1^2}{128}\big(1+\cos(\varphi_A-\varphi_B)\big)], \tag{A58}$$

which depends only on the phase difference $\varphi_A - \varphi_B$. This result corresponds to the case where the two RF photons are emitted at sequential times (early and late) and traverse the Franson interferometer via the short–long and long–short paths. The resulting $\cos(\varphi_A - \varphi_B)$ dependence is characteristic of post-selected time-bin entanglement.

2. For $F = 1$, the coherent field has a mean photon number $\mu = p_1/p_0$. The coincidence rate reduces to

$$\begin{aligned}\mathcal{C}(0)(\varphi_A,\varphi_B) = \frac{p_1^2}{256\,p_0^2}\Big[&(2p_0^2-4p_0+4)+(4p_0^2-8p_0+4)(\cos\varphi_A+\cos\varphi_B)\\ &+(2p_0^2-4p_0+2)\cos(\varphi_A-\varphi_B)+(8p_0^2-8p_0+2)\cos(\varphi_A+\varphi_B).\end{aligned} \tag{A59}$$

In addition to the $\cos(\varphi_A - \varphi_B)$ term from different-path interference, this expression also contains a $\cos(\varphi_A + \varphi_B)$ term, which originates from two photons taking the same path (short–short and long–long). Their relative weights are modulated by the parameter p_0. When the vacuum component in the resonance-fluorescence field dominates (i.e., p_0 is close to unity, corresponding to a weak excitation regime), the above equation simplifies dramatically to

$$\mathcal{C}(0)(\varphi_A, \varphi_B) = \frac{p_1^2}{128}(1 + \cos(\varphi_A + \varphi_B)), \tag{A60}$$

which shows that the interference pattern is governed solely by the sum phase $\varphi_A + \varphi_B$, while the difference phase cancels out completely. This sum-phase dependence demonstrates two-photon time-energy entanglement by a Franson interferometer.

3. Then, we consider the coincidence rate of the cases where the eigenvalue F = 2

$$\begin{aligned}\mathcal{C}(0)(\varphi_A, \varphi_B) = \frac{p_1^2}{256\, p_0^2}\Big[&(18p_0^2 - 80p_0 + 64) + (32p_0^2 - 96p_0 + 64)(\cos\varphi_A + \cos\varphi_B) \\ &+ (18p_0^2 - 48p_0 + 32)\cos(\varphi_A - \varphi_B) + (32p_0^2 - 64p_0 + 32)\cos(\varphi_A + \varphi_B)\Big].\end{aligned} \tag{A61}$$

In the weak-excitation limit ($p_0 \to 1$), the above equation reduces to

$$\mathcal{C}(0)(\varphi_A, \varphi_B) = \frac{p_1^2}{128}[1 + \cos(\varphi_A - \varphi_B)].$$

This result shows that at $F = 2$, the Franson interference pattern reverts to a phase-difference dependence, characteristic of time-bin entanglement and formally identical to the pure RF case at $F = 0$. By contrast, at $F = 1$ the phase-sum dependence signals energy-time entanglement.

4. Finally, we consider the asymptotic limit of a very large coherent amplitude, $F \to \infty$. In this regime, the dominant contribution in Equation (A56) comes from the F^4 term

$$\mathcal{C}(0)(\varphi_A, \varphi_B) \propto \frac{p_1^2 F^4}{64 p_0^2}(1 + \cos\varphi_A)(1 + \cos\varphi_B). \tag{A62}$$

This factorization indicates that in the strong laser drive, the two-photon coincidence rate becomes proportional to the product of the two individual single-photon rates.

Appendix D. Analytical Evaluation of the CHSH Bell Parameter

Using the coincidence rate $\mathcal{C}(0)(F, \theta, \varphi_A, \varphi_B)$ derived in Equation (A56), we define the normalized correlation function as

$$E(\varphi_A, \varphi_B) = \frac{\mathcal{C}(0)(\varphi_A, \varphi_B) + \mathcal{C}(0)(\varphi_A + \pi, \varphi_B + \pi) - \mathcal{C}(0)(\varphi_A + \pi, \varphi_B) - \mathcal{C}(0)(\varphi_A, \varphi_B + \pi)}{\mathcal{C}(0)(\varphi_A, \varphi_B) + \mathcal{C}(0)(\varphi_A + \pi, \varphi_B + \pi) + \mathcal{C}(0)(\varphi_A + \pi, \varphi_B) + \mathcal{C}(0)(\varphi_A, \varphi_B + \pi)}. \tag{A63}$$

The CHSH parameter is

$$S = \left|E(\varphi_A, \varphi_B) - E(\varphi_A, \varphi'_B) + E(\varphi'_A, \varphi_B) + E(\varphi'_A, \varphi'_B)\right|. \tag{A64}$$

Equation (A56) can be rearranged as

$$\mathcal{C}(0)(\varphi_A, \varphi_B) = \frac{p_1^2}{256}[\mathcal{A}_0 + \mathcal{A}_1(\cos\varphi_A + \cos\varphi_B) + \mathcal{A}_-\cos(\varphi_A - \varphi_B) + \mathcal{A}_+\cos(\varphi_A + \varphi_B)], \tag{A65}$$

where the coefficient $\mathcal{A}_1$ does not contribute to Equation (A63), and

$$\begin{aligned}\mathcal{A}_0 &= 2 + 8F\cos\theta + F^2\left(\frac{12}{p_0} + 4 + 4\cos 2\theta\right) + \frac{16F^3}{p_0}\cos\theta + \frac{4F^4}{p_0^2},\\ \mathcal{A}_- &= 2 + 8F\cos\theta + F^2\left(\frac{4}{p_0} + 4 + 4\cos 2\theta\right) + \frac{8F^3}{p_0}\cos\theta + \frac{2F^4}{p_0^2},\\ \mathcal{A}_+ &= 8F^2 + \frac{8F^3}{p_0}\cos\theta + \frac{2F^4}{p_0^2}.\end{aligned} \tag{A66}$$

The local phase terms cancel in Equation (A63), giving

$$E(\varphi_A, \varphi_B) = \frac{\mathcal{A}_- \cos(\varphi_A - \varphi_B) + \mathcal{A}_+ \cos(\varphi_A + \varphi_B)}{\mathcal{A}_0}. \tag{A67}$$

Writing Equation (A67) as

$$E(\varphi_A, \varphi_B) = T_x \cos\varphi_A \cos\varphi_B + T_y \sin\varphi_A \sin\varphi_B, \tag{A68}$$

with

$$T_x = \frac{\mathcal{A}_- + \mathcal{A}_+}{\mathcal{A}_0}, \qquad T_y = \frac{\mathcal{A}_- - \mathcal{A}_+}{\mathcal{A}_0}, \tag{A69}$$

the maximal CHSH value is

$$S_{\max} = 2\sqrt{T_x^2 + T_y^2} = \frac{2\sqrt{2(\mathcal{A}_-^2 + \mathcal{A}_+^2)}}{\mathcal{A}_0}. \tag{A70}$$

Equation (A70) therefore gives the maximal CHSH parameter analytically for arbitrary F, θ, and p_0 within the present model.

We now focus on the destructive-interference condition $\theta = \pi$. In this case,

$$\mathcal{A}_- = \frac{2}{p_0^2}\left(F^2 - 2p_0F + p_0\right)^2, \qquad \mathcal{A}_+ = \frac{2F^2}{p_0^2}(F - 2p_0)^2, \tag{A71}$$

and

$$\mathcal{A}_0 = \mathcal{A}_- + \mathcal{A}_+ + \frac{8F^2(1 - p_0)}{p_0}. \tag{A72}$$

At $(\theta = \pi)$, the nonnegative coefficients $(\mathcal{A}_-)$ and $(\mathcal{A}_+)$ quantify the phase-difference and phase-sum contributions, respectively. We define the crossovers between the time-bin-dominated and energy–time-dominated regimes by $(\mathcal{A}_- = \mathcal{A}_+)$. Since

$$\mathcal{A}_- - \mathcal{A}+ = 2 - 8F + \frac{4F^2}{p_0},$$

the crossover positions are

$$F_{c,\pm} = p_0 \pm \sqrt{p_0^2 - \frac{p_0}{2}}, \qquad p_0 > \frac{1}{2}.$$

The phase-sum contribution dominates between these positions, whereas the phase-difference contribution dominates outside them. This criterion identifies the exchange of dominant interference contributions, rather than the $(S_{\max} = 2)$ threshold.

Then the Equation (A70) reduces to

$$S_{\max}(F, p_0) = \frac{2\sqrt{2\left[(F^2 - 2p_0F + p_0)^4 + F^4(F - 2p_0)^4\right]}}{(F^2 - 2p_0F + p_0)^2 + F^2(F - 2p_0)^2 + 4F^2p_0p_1}, \tag{A73}$$

where $p_0 + p_1 = 1$. In the weak-excitation limit, $p_0 \to 1$, we define

$$w_- = (F-1)^4, \qquad w_+ = F^2(F-2)^2. \tag{A74}$$

Equation (A67) then reduces to

$$E(\varphi_A, \varphi_B) = \frac{w_- \cos(\varphi_A - \varphi_B) + w_+ \cos(\varphi_A + \varphi_B)}{w_- + w_+}. \tag{A75}$$

Thus, w_- and w_+ quantify the relative contributions of the phase-difference and phase-sum correlations, respectively. Equivalently,

$$E(\varphi_A, \varphi_B) = \cos\varphi_A \cos\varphi_B + \eta(F) \sin\varphi_A \sin\varphi_B, \tag{A76}$$

where

$$\eta(F) = \frac{(F-1)^4 - F^2(F-2)^2}{(F-1)^4 + F^2(F-2)^2}. \tag{A77}$$

The corresponding maximal Bell parameter is therefore

$$S_{\max}(F) = 2\sqrt{1 + \eta(F)^2}. \tag{A78}$$

For $\theta = \pi$ and $p_0 \to 1$, Equation (A18) gives

$$g^{(2)}(0) = \frac{w_+}{w_-}. \tag{A79}$$

Thus, $\eta(F)$ can be expressed solely in terms of $g^{(2)}(0)$

$$\eta = \frac{1 - g^{(2)}(0)}{1 + g^{(2)}(0)}. \tag{A80}$$

Therefore, Equation (A78) reduces to

$$S_{\max} = 2\sqrt{1 + \left[\frac{1 - g^{(2)}(0)}{1 + g^{(2)}(0)}\right]^2}. \tag{A81}$$

Equation (A81) establishes a direct connection between the CHSH parameter and the photon statistics in the weak-excitation limit. When $g^{(2)}(0) = 0$, we have $\eta = 1$ and $S_{\max} = 2\sqrt{2}$. From $g^{(2)}(0) = w_+/w_- = 0$ we obtain $F = 0$ and $F = 2$ for $p_0 \to 1$. The point $F = 0$ corresponds to pure RF input and is independent of p_1. When $g^{(2)}(0) \to \infty$, i.e., $w_- = 0$, we have $\eta \to -1$ and $S_{\max} = 2\sqrt{2}$. This occurs at $F = 1$ for $p_0 \to 1$. When $g^{(2)}(0) = 1$, we have $\eta = 0$ and $S_{\max} = 2$. From $g^{(2)}(0) = 1$, i.e., $w_+ = w_-$, we obtain $(F-1)^4 = F^2(F-2)^2$, whose solutions are $F_\pm = 1 \pm \frac{1}{\sqrt{2}} \simeq 0.29,\ 1.71$. At these points, $E(\phi_A, \phi_B) = \cos\phi_A \cos\phi_B$, so the correlation factorizes and $S_{\max} = 2$. Thus, in the weak-excitation limit, the maxima of S occur at $g^{(2)}(0) = 0$ ($F = 0$ and $F = 2$) and $g^{(2)}(0) \to \infty$ ($F = 1$), while the minima occur at $g^{(2)}(0) = 1$ ($F \simeq 0.29$ and 1.71).

Appendix E. Effect of Interference Contrast on the CHSH Parameter

Experimental imperfections can reduce the measured interference contrast through different mechanisms. Phase fluctuations wash out fringes upon averaging, pure dephasing reduces optical coherence, and beam-splitter imbalance can produce unequal amplitudes for interfering alternatives. Finite detector timing resolution can also reduce the contrast when distinct temporal contributions are mixed within the selected coincidence window. To assess the sensitivity of our predictions to this common effect, we introduce a phenomenological interference-contrast attenuation factor V_0, with $0 \leq V_0 \leq 1$, specifying the fraction of the ideal interference contrast retained.

Starting from Appendix D, we assume that the phase-difference and phase-sum interference terms in the coincidence rates are multiplied by the same factor V_0, while the phase-independent background remains unchanged. Applying the same coincidence normalization yields

$$E_{V_0}(\varphi_A, \varphi_B) = V_0 \frac{A_- \cos(\varphi_A - \varphi_B) + A_+ \cos(\varphi_A + \varphi_B)}{A_0} = V_0 E_{\text{ideal}}(\varphi_A, \varphi_B). \tag{A82}$$

Here, $V_0 = 1$ recovers the ideal correlation function, whereas $V_0 = 0$ removes both interference contributions.

For a fixed set of analyzer phases, the CHSH parameter is the absolute value of a linear combination of four correlation functions. If V_0 is independent of these phases, it factors out of both this combination and its maximization. Therefore,

$$S_{\max}(F, V_0) = V_0 S_{\max}^{\text{ideal}}(F), \tag{A83}$$

with all other parameters held fixed. For $V_0 > 0$, the ideal optimal analyzer settings remain optimal in this model.

The condition for the calculated postselected CHSH parameter to exceed 2 is consequently

$$V_0 > \frac{2}{S_{\max}^{\text{ideal}}(F)}. \tag{A84}$$

This condition is attainable only where $S_{\max}^{\text{ideal}}(F) > 2$. If the ideal value reaches $2\sqrt{2}$, the requirement reduces to $V_0 > 1/\sqrt{2} \approx 0.71$; lower ideal values require higher retained contrast. For a fixed $V_0 > 0$, the surviving intervals are precisely those satisfying $S_{\max}^{\text{ideal}}(F) > 2/V_0$. Thus, decreasing contrast progressively restricts the parameter regions with postselected CHSH values above 2.

Appendix F. Reference Simulation in the Ideal Weak-Excitation Limit

In the main text, we use $p_1 = 0.01$ as a practical weak-excitation condition. This choice preserves high first-order coherence while maintaining an experimentally useful RF photon flux. To make the underlying interference mechanism more transparent, we also consider here a much weaker excitation condition with

$$p_1 = 10^{-6}, \qquad p_0 \simeq 1. \tag{A85}$$

Using $p_1 = \frac{2\Omega^2 T_1^2}{1+2\Omega^2 T_1^2}$, this corresponds to $\Omega T_1 \simeq 7.1 \times 10^{-4}$. This regime is not intended as a practical operating point because of the low RF photon flux. Its purpose is instead to expose the limiting physics of RF–laser interference.

Figure A1a shows the first-order coherence $|g^{(1)}(\tau)|$ for $\theta = \pi$. Because $p_0 \simeq 1$, the coherence remains essentially unity except in a very narrow region around $F = p_0 \simeq 1$,

where the phase-coherent RF and laser amplitudes cancel. This narrow dip illustrates the ideal homodyne cancellation condition more sharply than in the practical case $p_1 = 0.01$.

Figure A1b shows the CHSH Bell parameter S as a function of the relative field amplitude F for $\theta = \pi$. In this ideal weak-excitation regime, the curve approaches the analytic limits discussed in the main text. The Bell parameter reaches values close to $2\sqrt{2}$ at $F = 0$, $F = 1$, and $F = 2$, corresponding respectively to time-bin entanglement, energy–time entanglement, and recovered time-bin entanglement. Between these regimes, S falls to the classical bound near the points where $g^{(2)}(0) = 1$. For large F, the coherent field dominates and S approaches the classical limit $S = 2$.

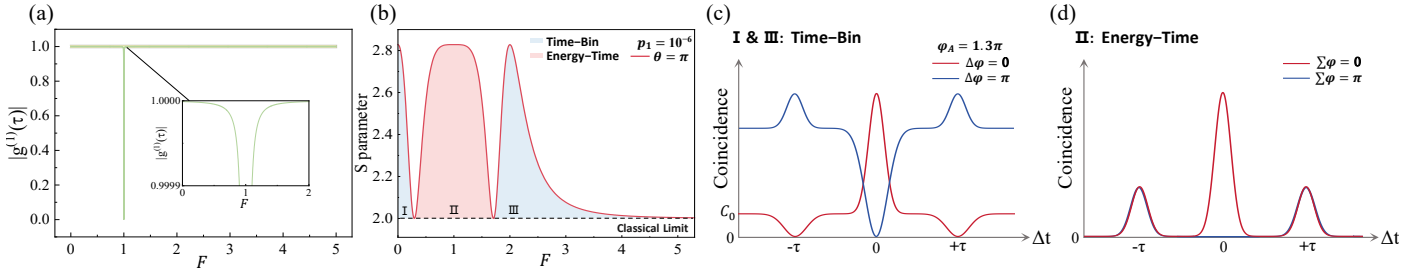


Figure A1. Reference simulation for $\theta = \pi$, with $p_1 = 10^{-6}$. (**a**) $|g^{(1)}(\tau)|$ as a function of F. Inset: a magnified view around $F = 1$. (**b**) CHSH Bell parameter S as a function of F. (**c**) Representative Franson coincidence histogram for the time-bin entanglement regimes at $F = 0$ and $F = 2$, where the zero-delay rate depends on $\Delta\varphi = \varphi_A - \varphi_B$. The two curves correspond to $(\varphi_A, \varphi_B) = (1.3\pi, 1.3\pi)$ and $(1.3\pi, 0.3\pi)$, i.e., $\Delta\varphi = 0$ and π. First-order coherence causes phase-dependent interference, so the baseline C_0 varies with the phase setting. (**d**) Representative Franson coincidence histogram for the energy–time entanglement regime at $F = 1$, where the zero-delay coincidence rate depends on $\Sigma\varphi = \varphi_A + \varphi_B$. The two curves correspond to $\Sigma\varphi = 0$ and π.

Figure A1c,d show representative Franson coincidence histograms expected for the two types of entanglement. For the time-bin entanglement regimes, corresponding to Regions I and III, the phase-dependent two-photon interference is governed by the phase difference $\Delta\varphi = \varphi_A - \varphi_B$. The relevant indistinguishable alternatives are the long–short and short–long paths of the two analysis AMZIs, giving coincidence profiles that switch between constructive and destructive interference as $\Delta\varphi$ is varied. In these regimes, both the zero-delay coincidence probability and the baseline coincidence probability scale as p_1^2. The baseline therefore remains finite relative to the zero-delay coincidence signal in the normalized histogram and, due to first-order interference, depends separately on the analyzer phases φ_A and φ_B, rather than on their difference $\Delta\varphi$ [17].

By contrast, in the energy–time entanglement regime of Region II, centered around $F = 1$, the single-photon component is canceled and the coincidence signal is dominated by the simultaneous two-photon component. The relevant indistinguishable alternatives are then the short–short and long–long paths, so that the interference depends on the phase sum $\Sigma\varphi = \varphi_A + \varphi_B$. The zero-delay Franson coincidence probability scales as p_1^2, whereas the baseline coincidence probability scales as p_1^4. The baseline is therefore negligible in the weak-excitation limit. These histograms thus provide a direct time-domain distinction between phase-difference interference in the time-bin regimes and phase-sum interference in the energy–time regime.

Overall, this idealized calculation provides a reference limit in which the three entangled regimes are clearly separated. It confirms that the finite-p_1 results in the main text are a practical realization of the same underlying sequence: time-bin entanglement, energy–time entanglement, and recovered time-bin entanglement, followed by the approach to classical coherent-field interference.

References

1. Bennett, C.H.; Brassard, G.; Crépeau, C.; Jozsa, R.; Peres, A.; Wootters, W.K. Teleporting an Unknown Quantum State via Dual Classical and Einstein–Podolsky–Rosen Channels. *Phys. Rev. Lett.* **1993**, *70*, 1895–1899.
2. Bennett, C.H.; Brassard, G.; Popescu, S.; Schumacher, B.; Smolin, J.A.; Wootters, W.K. Purification of Noisy Entanglement and Faithful Teleportation via Noisy Channels. *Phys. Rev. Lett.* **1996**, *76*, 722–725.
3. Ekert, A.K. Quantum Cryptography Based on Bell's Theorem. *Phys. Rev. Lett.* **1991**, *67*, 661–663.
4. Brendel, J.; Gisin, N.; Tittel, W.; Zbinden, H. Pulsed Energy-Time Entangled Twin-Photon Source for Quantum Communication. *Phys. Rev. Lett.* **1999**, *82*, 2594–2597.
5. Duan, L.M.; Lukin, M.D.; Cirac, J.I.; Zoller, P. Long-distance quantum communication with atomic ensembles and linear optics. *Nature* **2001**, *414*, 413–418.
6. Bennett, C.H.; DiVincenzo, D.P. Quantum information and computation. *Nature* **2000**, *404*, 247–255.
7. Knill, E.; Laflamme, R.; Milburn, G.J. A scheme for efficient quantum computation with linear optics. *Nature* **2001**, *409*, 46–52.
8. Kok, P.; Munro, W.J.; Nemoto, K.; Ralph, T.C.; Dowling, J.P.; Milburn, G.J. Linear optical quantum computing with photonic qubits. *Rev. Mod. Phys.* **2007**, *79*, 135–174.
9. Giovannetti, V.; Lloyd, S.; Maccone, L. Advances in quantum metrology. *Nat. Photon.* **2011**, *5*, 222–229.
10. Kwiat, P.G.; Mattle, K.; Weinfurter, H.; Zeilinger, A.; Sergienko, A.V.; Shih, Y. New High-Intensity Source of Polarization-Entangled Photon Pairs. *Phys. Rev. Lett.* **1995**, *75*, 4337–4341.
11. Li, X.; Voss, P.L.; Sharping, J.E.; Kumar, P. Optical-Fiber Source of Polarization-Entangled Photons in the 1550 nm Telecom Band. *Phys. Rev. Lett.* **2005**, *94*, 053601.
12. Takesue, H.; Inoue, K. Generation of 1.5-μm band time-bin entanglement using spontaneous fiber four-wave mixing and planar lightwave circuit interferometers. *Phys. Rev. A* **2005**, *72*, 041804(R).
13. Bouwmeester, D.; Pan, J.W.; Mattle, K.; Eibl, M.; Weinfurter, H.; Zeilinger, A. Experimental quantum teleportation. *Nature* **1997**, *390*, 575–579.
14. Walther, P.; Resch, K.J.; Rudolph, T.; Schenck, E.; Weinfurter, H.; Vedral, V.; Aspelmeyer, M.; Zeilinger, A. Experimental one-way quantum computing. *Nature* **2005**, *434*, 169–176.
15. Pan, J.W.; Chen, Z.B.; Lu, C.Y.; Weinfurter, H.; Zeilinger, A.; Żukowski, M. Multiphoton entanglement and interferometry. *Rev. Mod. Phys.* **2012**, *84*, 777–838.
16. Zhong, H.S.; Li, Y.; Li, W.; Peng, L.C.; Su, Z.E.; Hu, Y.; He, Y.M.; Ding, X.; Zhang, W.; Li, H.; et al. 12-Photon Entanglement and Scalable Scattershot Boson Sampling with Optimal Entangled-Photon Pairs from Parametric Down-Conversion. *Phys. Rev. Lett.* **2018**, *121*, 250505.
17. Zeng, Z.Q.; Wang, J.; Liu, X.B.; Wang, X.J.; Liu, L.; Liu, H.; Ni, H.; Niu, Z.; Antón-Solanas, C.; Wu, B.; et al. Bell inequality violation with vacuum–one-photon number superposition states. *Optica* **2026**, *13*, 2306–2311.
18. Peiris, M.; Konthasinghe, K.; Müller, A. Franson interference generated by a two-level system. *Phys. Rev. Lett.* **2017**, *118*, 030501.
19. Liu, S.; Sandberg, O.A.D.; Chan, M.L.; Schrinski, B.; Anyfantaki, Y.; Nielsen, R.B.; Larsen, R.G.; Skalkin, A.; Wang, Y.; Midolo, L.; et al. Violation of Bell inequality by photon scattering on a two-level emitter. *Nat. Phys.* **2024**, *20*, 1429–1433.
20. Wang, J.; Liu, X.B.; Zeng, Z.; Wang, X.J.; Antón-Solanas, C.; Liu, L.; Liu, H.; Ni, H.; Niu, Z.; Wu, B.; et al. Engineering energy-time entanglement from resonance fluorescence. *arXiv* **2026**, arXiv:2603.25341. https://doi.org/10.48550/arXiv.2603.25341.
21. Höffges, J.; Baldauf, H.; Eichler, T.; Helmfrid, S.; Walther, H. Heterodyne measurement of the fluorescent radiation of a single trapped ion. *Opt. Commun.* **1997**, *133*, 170–174.
22. Nguyen, H.S.; Sallen, G.; Voisin, C.; Roussignol, P.; Diederichs, C.; Cassabois, G. Ultra-coherent single photon source. *Appl. Phys. Lett.* **2011**, *99*, 261904.
23. Matthiesen, C.; Vamivakas, A.N.; Atatüre, M. Subnatural Linewidth Single Photons from a Quantum Dot. *Phys. Rev. Lett.* **2012**, *108*, 093602.
24. López Carreño, J.C.; Casalengua, E.Z.; Laussy, F.P.; del Valle, E. Joint subnatural-linewidth and single-photon emission from resonance fluorescence. *Quantum Sci. Technol.* **2018**, *3*, 045001.
25. Wang, X.J.; Huang, G.; Li, M.Y.; Wang, Y.Z.; Liu, L.; Wu, B.; Liu, H.; Ni, H.; Niu, Z.; Ji, W.; et al. Coherence in resonance fluorescence. *Nat. Commun.* **2025**, *16*, 6453.
26. Huang, G.; Wang, J.; Zeng, Z.; Liu, H.; Liu, L.; Ji, W.; Wu, B.; Ni, H.; Niu, Z.; Jiao, R.; et al. Two-photon interference between mutually detuned resonance-fluorescence signals scattered off a semiconductor quantum dot. *Phys. Rev. A* **2026**, *113*, 023718.
27. Franson, J.D. Bell Inequality for Position and Time. *Phys. Rev. Lett.* **1989**, *62*, 2205–2208.
28. Clauser, J.F.; Horne, M.A.; Shimony, A.; Holt, R.A. Proposed Experiment to Test Local Hidden-Variable Theories. *Phys. Rev. Lett.* **1969**, *23*, 880–884.
29. Kim, S.K.; Casalengua, E.Z.; Boos, K.; Sbresny, F.; Calcagno, C.; Riedl, H.; Finley, J.J.; Antón-Solanas, C.; Laussy, F.P.; Müller, K.; et al. Unlocking multiphoton emission from a single-photon source through mean-field engineering. *Sci. Adv.* **2025**, *11*, eadw3395.

30. Bracht, T.K.; Clark, R.N.; Androvitsaneas, P.; Jordan, M.; Bishop, S.G.; Dyte, H.E.; Cygorek, M.; Farrer, I.A.; Reiter, D.E.; Bennett, A.J. Tunable multi-photon correlations from a coherently driven quantum dot. *Opt. Quantum* **2026**, *4*, 224–231.
31. Yin, H.L.; Liu, R.Z.; Lyu, S.T.; Yuan, Z. Tunable high-order coherence in the interference of resonance fluorescence and laser light. *Opt. Let.* **2026**, *51*, 2616–2619.
32. Wu, B.; Wang, X.J.; Liu, L.; Huang, G.; Wang, W.; Liu, H.; Ni, H.; Niu, Z.; Yuan, Z. Mollow Triplets under Few-Photon Excitation. *Optica* **2023**, *10*, 1118–1123.

Disclaimer/Publisher's Note: The statements, opinions and data contained in all publications are solely those of the individual author(s) and contributor(s) and not of MDPI and/or the editor(s). MDPI and/or the editor(s) disclaim responsibility for any injury to people or property resulting from any ideas, methods, instructions or products referred to in the content.